# Magnetism and its coexistence with superconductivity in $CaK(Fe_{0.949}Ni_{0.051})_4As_4$: Muon spin rotation/relaxation studies

Rustem Khasanov [1,*], Gediminas Simutis [1,2], Yurii G. Pashkevich [3], Tatyana Shevtsova,[3] William R. Meier,[4,5]
Mingyu Xu,[4,5] Sergey L. Bud'ko,[4,5] Vladimir G. Kogan,[4] and Paul C. Canfield [4,5]

[1]*Laboratory for Muon Spin Spectroscopy, Paul Scherrer Institut, CH-5232 Villigen PSI, Switzerland*
[2]*Laboratoire de Physique des Solides, CNRS, Université Paris-Sud, Université Paris-Saclay, 91405 Orsay Cedex, France*
[3]*O. O. Galkin Donetsk Institute for Physics and Engineering NAS of Ukraine, 03680 Kyiv-Kharkiv, Ukraine*
[4]*Division of Materials Science and Engineering, Ames Laboratory, Ames, Iowa 50011, USA*
[5]*Department of Physics and Astronomy, Iowa State University, Ames, Iowa 50011, USA*

The magnetic response of $CaK(Fe_{0.949}Ni_{0.051})_4As_4$ was investigated by means of the muon spin rotation/relaxation. The long-range commensurate magnetic order sets in below the Néel temperature $T_N = 50.0(5)$ K. The density-functional theory calculations have identified three possible muon stopping sites. The experimental data were found to be consistent with only one type of magnetic structure, namely, the long-range magnetic spin-vortex-crystal order with the hedgehog motif within the $ab$ plane and the antiferromagnetic stacking along the $c$ direction. The value of the ordered magnetic moment at $T \approx 3$ K was estimated to be $m_{Fe} = 0.38(11)\mu_B$ ($\mu_B$ is the Bohr magneton). A microscopic coexistence of magnetic and superconducting phases accompanied by a reduction of the magnetic order parameter below the superconducting transition temperature $T_c \simeq 9$ K is observed. Comparison with 11, 122, and 1144 families of Fe-based pnictides points to existence of correlation between the reduction of the magnetic order parameter at $T \to 0$ and the ratio of the transition temperatures $T_c/T_N$. Such correlations were found to be described by Machida's model for coexistence of itinerant spin-density-wave magnetism and superconductivity [K. Machida, J. Phys. Soc. Jpn. **50**, 2195 (1981); S. L. Bud'ko *et al.*, Phys. Rev. B **98**, 144520 (2018)].

## I. INTRODUCTION

Since their discovery, iron-based superconductors (Fe-SC's) have attracted much interest. The materials belonging to various classes of Fe-SC's were found to be characterized by unconventional superconducting properties, as well as by a strong interplay of superconductivity with various electronic ground states such as, e.g., nematic phase and spin-density-wave magnetism [1–7]. All Fe-SC's have a layered structure and share a common $Fe_2An_2$ ($An =$ P, As, Se, Te) layers (see also Fig. 1), analogous to the $CuO_2$ sheets in high-temperature cuprates [8].

Recently, a new, 1144 Fe-SC family ($AeAFe_4As_4$, $Ae =$ Ca, Sr, Eu and $A =$ K, Rb, Cs), with the transition temperature $T_c$ reaching $\simeq 36$ K, was synthesized [9–12]. The crystallographic structure of $AeAFe_4As_4$ (see, e.g., Fig. 1 for $CaKFe_4As_4$ representative of 1144 family) is different compared to intensively studied materials belonging to 122 family of Fe-SC's. The $Ae$ and $A$ sites form alternating planes along the crystallographic $c$ axis and are separated by $Fe_2As_2$ layers. There are two distinct As sites, As1 and As2, neighboring K and Ca, respectively, rather than one As site found in $CaFe_2As_2$ and $KFe_2As_2$ (see Fig. 1). Partial substitution of Fe by Co or Ni in $CaKFe_4As_4$ (electron doping) shift the

ground state from superconducting to antiferromagnetically (AFM) ordered [11–13]. The resistivity and the specific-heat measurements [10–12], as well as the Mössbauer [13,14], the nuclear magnetic resonance (NMR) [13], and the neutron scattering studies [15] reveal the appearance of a magnetic order. The magnetism was further identified as the hedgehog spin-vortex-crystal (SVC) order, which is characterized by noncollinear Fe moments featuring an alternating all-in and all-out motif around the As1 sites within the $ab$ planes and antiferromagnetic coupling along the $c$ direction [13,15]. In addition, the interplay of magnetism and superconductivity in $CaK(Fe_{1-x}Ni_x)_4As_4$ was clearly detected in NMR, Mössbauer spectroscopy, and neutron scattering experiments [10–16]. As both states compete for the same electrons at the Fermi surface, the magnetic order parameter was found to be strongly reduced below $T_c$.

This paper reports the results of the muon spin rotation/relaxation ($\mu$SR) studies of $CaK(Fe_{0.949}Ni_{0.051})_4As_4$ single-crystal sample. The density-functional theory calculations have identified three possible muon stopping sites. The experimental data were found to be consistent with only one type of the magnetic structure, namely, the long-range magnetic spin-vortex-crystal order with the hedgehog motif within the $ab$ plane and the AFM stacking along the $c$ direction. The value of the ordered magnetic moment at $T \approx 3$ K was estimated to be $m_{Fe} = 0.38(11)\mu_B$ ($\mu_B$ is the Bohr magneton). All these results stay in agreement with those published
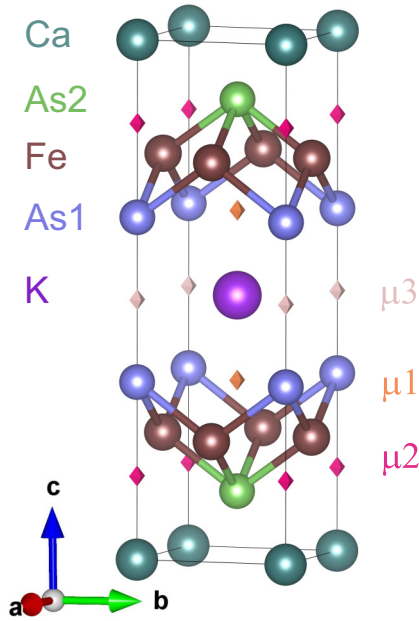
*rustem.khasanov@psi.ch

FIG. 1. The crystal structure of CaKFe$_4$As$_4$ within the $P4/mmm$ group representation. Three muon stopping sites (denoted by diamonds) are $\mu 1$, the Wyckoff position is (0.5,0.5,0.301), the local symmetry is 2$h$; $\mu 2$, the Wyckoff position is (0,0,0.186), the local symmetry is 2$g$; and $\mu 3$, the Wyckoff position is (0,0,0.5), the local symmetry is 1$b$. The crystal structure is visualized by using the VESTA package [18].

previously in Refs. [12–15]. The temperature evolution of the magnetic order parameter $m_{\mathrm{Fe}}(T)$ was analyzed by using the approach of Machida [14,17], accounting for coexistence of a spin-density-wave magnetism and superconductivity. The theory results of Refs. [14,17] were further extended for studying the superconductivity induced suppression of the magnetic order parameter in the limit of $T \to 0$.

The paper is organized as follows. The experimental details, including the sample preparation procedure, the description of $\mu$SR setup and the details of the muon-site calculations are given in Sec. II. The results of the weak transverse-field and zero-field $\mu$SR experiments are presented in Sec. III. Section IV discusses the experimental data. Conclusions follow in Sec. V. Appendices A and B describe the results of calculations of the dipolar fields at the muon stopping sites and extensions of Machida's theory at the limit of $T \to 0$, respectively.

## II. EXPERIMENTAL DETAILS

### A. Sample preparation and characterization

CaK(Fe$_{0.949}$Ni$_{0.051}$)$_4$As$_4$ single crystals were grown from a high-temperature Fe-As rich melt and extensively characterized by thermodynamic and transport measurements [10–15]. The selected crystal with dimensions of $\simeq 4.0 \times 4.0 \times 0.1$ mm$^3$ was used. The magnetic ordering temperature $T_{\mathrm{N}} \simeq 50.6(5)$ and the superconducting transition temperature $T_{\mathrm{c}} \simeq 9.0(8)$ K, for CaK(Fe$_{0.949}$Ni$_{0.051}$)$_4$As$_4$ single crystals from the same grown batch, were inferred from temperature-dependent
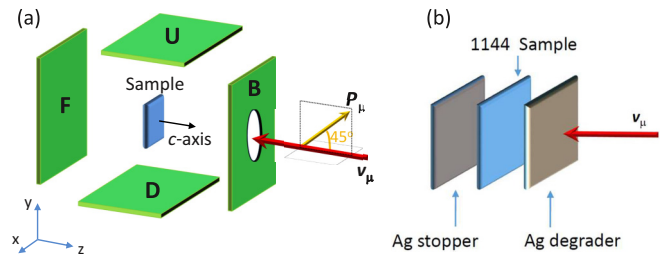


FIG. 2. (a) The schematic representation of an arrangement of positron counters at the GPS (General Purpose Surface) spectrometer at the Paul Scherrer Institute, Switzerland [19]. The letters F, B, U, and D denote the forward, backward, up, and down detectors, respectively. The single-crystalline sample (blue rectangle) has its $c$ axis aligned along the incoming muon beam (red arrow). The initial muon spin polarization $P_\mu$ was rotated by 45$^\circ$ within the vertical ($y$-$z$) plane. (b) CaK(Fe$_{0.949}$Ni$_{0.051}$)$_4$As$_4$ sample sandwiched between Ag (degrader and stopper) sheets.

electrical-resistance, heat-capacity, and magnetization studies of Kreyssig *et al.* [15].

### B. Muon spin rotation/relaxation experiments

The muon spin rotation/relaxation ($\mu$SR) experiments were carried out at the $\pi$M3 beam line using the GPS (General Purpose Surface) spectrometer at the Paul Scherrer Institute, Switzerland [19]. The zero-field (ZF) and the weak transverse-field (wTF) $\mu$SR measurements were performed at temperatures ranging from $\simeq 1.5$ to 100 K. The 100% spin-polarized muons with the momentum of $\simeq 28.6$ MeV/c were implanted into the crystal along the $c$ axis (see Fig. 2). Muons thermalize rapidly without a significant loss of their initial spin polarization and stop in the matter at the depth of about 0.15 g/cm$^2$. For CaK(Fe$_{0.949}$Ni$_{0.051}$)$_4$As$_4$ with the density of $\simeq 5.2$ g/cm$^3$ this corresponds to a depth of $\simeq 0.3$ mm. In order to measure the sample with a thickness of $\simeq 0.1$ mm, as CaK(Fe$_{0.949}$Ni$_{0.051}$)$_4$As$_4$ single crystal studied here, a special sample holder described in Ref. [20] was used. The sample was sandwiched between silver sheets, with the first one playing a role of a "degrader" by decelerating the muons in the incoming muon beam and the second one as a "stopper" by stopping the muons which were still able to penetrate through the sample [see Fig. 2(b)]. The detailed description of $\mu$SR technique can be found, e.g., in Refs. [21–24].

The $\mu$SR experiments were performed in the so-called spin-rotated mode, i.e., when the initial muon spin polarization ($P_\mu$) is turned by a certain angle relative to the muon beam momentum [$v_\mu$, see Fig. 2(a)]. Such geometry is particularly suitable to perform experiments on single-crystalline samples since it allows to probe independently the time evolution of the "parallel" and "perpendicular" components of the muon spin polarization [$P(t)$] by accessing the response of the backward/forward (B/F) and up/down (U/D) positron counters. In a case of the single-crystalline CaK(Fe$_{0.949}$Ni$_{0.051}$)$_4$As$_4$ sample with the $c$ axis aligned along the muon momentum (see Fig. 2) the up/down and backward/forward counters access the $P^{\perp c}(t)$ and $P^{\parallel c}(t)$ components of the muon spin polarization, respectively.

The experimental data were analyzed by using the MUSRFIT package [25]. The typical counting statistics were $\simeq 2 \times 10^7$ and $3 \times 10^6$ positron events for ZF and wTF experiments, respectively.

### C. Muon stopping positions

The muon stopping sites can be identified as a local interstitial minima of the valence electron electrostatic potential which can be further restored from the electron density distribution. In order to find them, *ab initio* calculations within the framework of density-functional theory were performed. As the initial structural data, the $P4/mmm$ space-group symmetry of CaKFe$_4$As$_4$ with one formula unit ($Z = 1$) was considered (see Fig. 1). The Ca ions reside at $1a$ Wyckoff position (0,0,0), K at the $1d$ position (0.5,0.5,0.5), Fe at the $4i$ position (0,0.5,0.76820), As1 at the $2g$ position (0,0,0.34150), and As2 at the $2h$ position (0.5,0.5,0.12310). The lattice constants were taken to be $a = 3.8659$ Å and $c = 12.8840$ Å [11,12]. The all-electron full-potential linearized augmented plane-wave method (ELK code) [26], with the local spin-density approximation [27], for the exchange correlation potential and with the revised generalized gradient approximation of Perdew-Burke-Ernzerhof [28] was applied. The calculations were performed on a $13 \times 13 \times 4$ grid which corresponds to 84 points in the irreducible Brillouin zone.

Three types of possible muon positions were detected (see Fig. 1). The first one ($\mu$1) stays in-between K-As2 ions and has coordinates (0.5,0.5,0.301). The local symmetry of this position is $2h$. Two other positions are located on the line along the $c$ direction connecting the nearest Ca-As1-As1-Ca ions. The local symmetries and positions are $\mu$2-$2g$ (0,0,0.186) and $\mu$3-$1b$ (0,0,0.5). The positions $\mu$1 and $\mu$2 have the same local symmetry ($2g$ and $2h$) as they were found in Ba$_{1-x}$A$_x$Fe$_2$As$_2$ [29,30]. The occupancy of the muon sites decreases from the site $\mu$1 to the site $\mu$3 ($\mu$1 $\rightarrow$ $\mu$2 $\rightarrow$ $\mu$3), as it follows from the ratio of corresponding electrostatic potentials: $(-\varphi_{\mu 1})/(-\varphi_{\mu 2})/(-\varphi_{\mu 3}) \simeq 1.00/0.96/0.93$. Two points need to be mentioned: (i) Few muon stopping positions with a much higher electrostatic potentials were assumed to be unoccupied by muons and, therefore, not considered. (ii) It is assumed that the muon sites calculated for CaKFe$_4$As$_4$ do not strongly change under the low level of Fe to Ni replacement.

## III. RESULTS

### A. Weak transverse-field $\mu$SR experiments

$\mu$SR experiments under weak transverse-field (wTF) applied perpendicular to the muon spin polarization are a straightforward method to determine the onset of the magnetic transition and the magnetic volume fraction. In this case, the contribution to the asymmetry from muons experiencing a vanishing internal spontaneous magnetization can be accurately determined. Muons stopping in a nonmagnetic environment produce long-lived oscillations, which reflect the coherent muon precession around the external field $B_{ex}$. Muons stopping in magnetically ordered parts of the sample give rise to a more complex, distinguishable signal, reflecting the vector combination of internal and external fields.
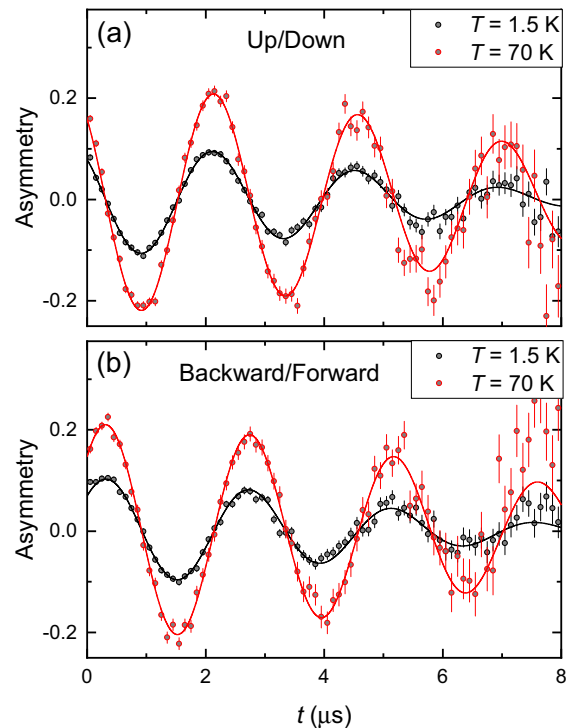


FIG. 3. (a) WTF-$\mu$SR time spectra ($B_{ex} = 3$ mT) of CaK(Fe$_{0.949}$Ni$_{0.051}$)$_4$As$_4$ measured on up/down set of positron counters below ($T \simeq 1.5$ K) and above ($T = 70$ K) the magnetic transition temperature ($T_N \simeq 50$ K). The solid lines are fits of Eq. (3) to the data (see text for details). (b) The same as (a) but for backward/forward set of detectors.

Figure 3 shows the wTF-$\mu$SR time spectra of CaK(Fe$_{0.949}$Ni$_{0.051}$)$_4$As$_4$ single-crystal sample measured above ($T \simeq 70$ K) and below ($T \simeq 1.5$ K) the magnetic transition ($T_N \simeq 50$ K). The external magnetic field $B_{ex} = 3$ mT was applied along the $x$ direction [see Fig. 2(a)]. The angle between the initial muon spin polarization and the muon momentum was set to 45°. Figures 3(a) and 3(b) correspond to the data collected on up/down and backward/forward set of detectors.

The time evolution of the muon spin asymmetry in $\mu$SR experiments $A(t)$ can be described as

$$A(t) = A(0)P(t) = A_s(0)P_s(t) + A_{bg}(0)P_{bg}(t). \quad (1)$$

Here, the indices "s" and "bg" denote the sample and background contributions, respectively. $A_s(0)$ [$A_{bg}(0)$] are the initial asymmetry and $P_s(t)$ [$P_{bg}(t)$] the time evolution of the muon spin polarization belonging to the sample (background). The background component represents the muons missing the sample and stopped, e.g., in Ag degrader sheets [see Fig. 2(b)], cryostat walls, cryostat windows, etc. Considering the transition of CaK(Fe$_{0.949}$Ni$_{0.051}$)$_4$As$_4$ from nonmagnetic (nm) to the magnetic (m) state [12–15], the sample contribution was further assumed to consist of two parts [31]:

$$A_s(t) = A_{nm}(0)P_{nm}(t) + A_m(0)P_m(t). \quad (2)$$

In analysis of wTF-$\mu$SR data only the nonmagnetic sample component was considered. The magnetic term [$A_m(0)P_m(t)$] vanishes within the first $\sim$0.1 $\mu$s (see Sec. IIIB1) and thus it is
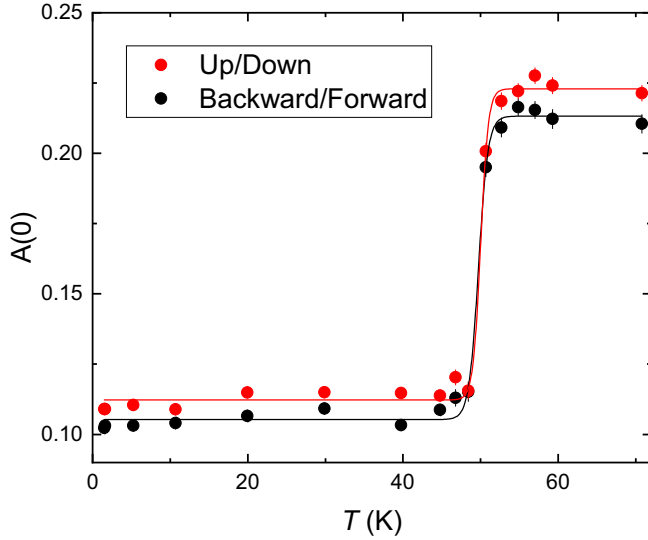
FIG. 4. Temperature dependencies of the initial asymmetry $A(0)$ for the up/down and backward/forward set of positron counters. The solid lines are fits of Eq. (4) to $A(0)$ vs $T$ data. See text for details.

not observed with the present data binning ($\simeq 0.126$ $\mu$s). The "nm" and "bg" contributions in Eqs. (1) and (2) were further combined into the single term

$$A(t) = A(0) \cos(\gamma_\mu B_{ex} t + \phi) e^{-\sigma^2 t^2/2}. \qquad (3)$$

Here, $\phi$ is the initial phase of the muon spin ensemble, and $\sigma$ is the Gaussian relaxation rate. The solid lines in Fig. 3 correspond to the fit of Eq. (3) to the wTF-$\mu$SR data.

Figure 4 shows the temperature dependence of the initial asymmetry $A(0)$ obtained from the fit of wTF-$\mu$SR data by means of Eq. (3). The magnetic ordering temperature $T_N$ and the width of the magnetic transition $\Delta T_N$ were determined by using the phenomenological function [32]

$$A(0, T) = A_s(0) \frac{1}{1 + \exp([T_N - T]/\Delta T_N)} + A_{bg}(0). \qquad (4)$$

The results of the fit are represented by solid lines. The fit results for the up/down (backward/forward) set of detectors are $T_N = 50.0(2)$ K [49.7(2) K], $\Delta T = 0.5(1)$ K [0.6(1) K], $A_s(0) = 0.111(2)$ [0.108(2)], and $A_{bg}(0) = 0.112(1)$ [0.105(1)].

The results of wTF-$\mu$SR experiments can be summarized as follows:

(i) The value of the magnetic ordering temperature $T_N = 49.9(3)$ K coincides rather well with 50.0(6) K obtained by Kreyssig *et al.* [15] in resistivity, specific heat, and neutron scattering experiments on the sample with the similar doping level.

(ii) The width of the transition $\Delta T_N = 0.5(2)$ K is rather small suggesting that the magnetic order sets inside the sample uniformly. In other words, the magnetic ordering temperature $T_N$ stays the same (within $\simeq 0.5$ K accuracy) over the full sample volume.

(iii) The fact that $A_s(0) \simeq A_{bg}(0)$ implies that 50% of all the muons stop in the sample, while the rest contribute to the background.

### B. Zero-field $\mu$SR experiments

#### 1. $P^{\perp c}$ and $P^{\|c}$ set of data

In ZF-$\mu$SR experiments, the muon spin precesses in internal field(s) at the muon stopping site(s) which are created by the surrounding magnetic moments (nuclear or electronic in origin). Figure 5 shows the ZF-$\mu$SR time spectra collected on up/down [Fig. 5(a)] and backward/forward [Fig. 5(e)] set of positron counters. In order to improve statistics, the data sets collected at temperatures ranging from $\simeq 1.5$ up to 5 K are combined together. Obviously, oscillations of the muon spin polarization corresponding to the precession of the muon spin in internal field ($B_{int}$) are observed for the up/down, but they are missing for the backward/forward set of detectors. Bearing in mind that the up/down and backward/forward responses correspond to the time evolution of $P^{\perp c}$ and $P^{\|c}$ components of the muon spin polarization, respectively (see Sec. II B and Fig. 2), one concludes that internal fields on the muon stopping sites are aligned along the $c$ axis of the CaK(Fe$_{0.949}$Ni$_{0.051}$)$_4$As$_4$ single crystal.

The analysis of the sample response in ZF-$\mu$SR experiments was performed by considering the presence of three muon stopping sites as inferred from the muon site calculations (see Sec. II C and Fig. 1):

$$A_m^{ZF}(t) = \sum_{i=1}^{3} A_i(0) \, e^{-\sigma_i^2 t^2/2} \, \cos(\gamma_\mu B_{int,i} t). \qquad (5)$$

Here, $A_i(0)$, $\sigma_i$, and $B_{int,i}$ are the initial asymmetry, the Gaussian relaxation rate, and the internal field of the $i$th component, respectively. Fits of Eq. (1) with the sample part described by Eq. (5) to the ZF-$\mu$SR data are presented in Figs. 5(a) and 5(e) by solid red lines. The parameters obtained from the fits are summarized in Table I.

From the results of the fit, the following three important points emerge:

(i) Three components (two oscillating, No. 1 and No. 2, and one fast relaxing nonoscillating, No. 3) are clearly resolved by fitting the up/down ($P^{\perp c}$) set of data. The time evolutions of these components are presented in Figs. 5(b), 5(c), and 5(d).

(ii) The fit of the backward/forward ($P^{\|c}$) set of data could be performed by using only two components (the slow and the fast relaxing ones). The relative weight (the fraction) of the fast relaxing component is the *same* (within the experimental accuracy) as the nonoscillating fast relaxing one in the up/down ($P^{\perp c}$) set of data. It is reasonable to assume, therefore, that in both set of experiments the nonoscillating fast relaxing component (No. 3) originates from the same muon stopping site. The slow relaxing contribution was further assigned to two oscillating components (No. 1 and No. 2) observed in up/down set of positron counters.

(iii) The ratio between the sample and the background asymmetries was fixed to that determined in wTF experiments [$A_s(0) \simeq A_{bg}(0) \simeq 0.5A(0)$]. The time evolution of the background component is presented in Figs. 5(a) and 5(e) by dashed lines.

#### 2. Temperature dependence of the internal field $B_{int}$

The value of the internal field at the muon stopping position is determined by surrounding magnetic moments. In a case
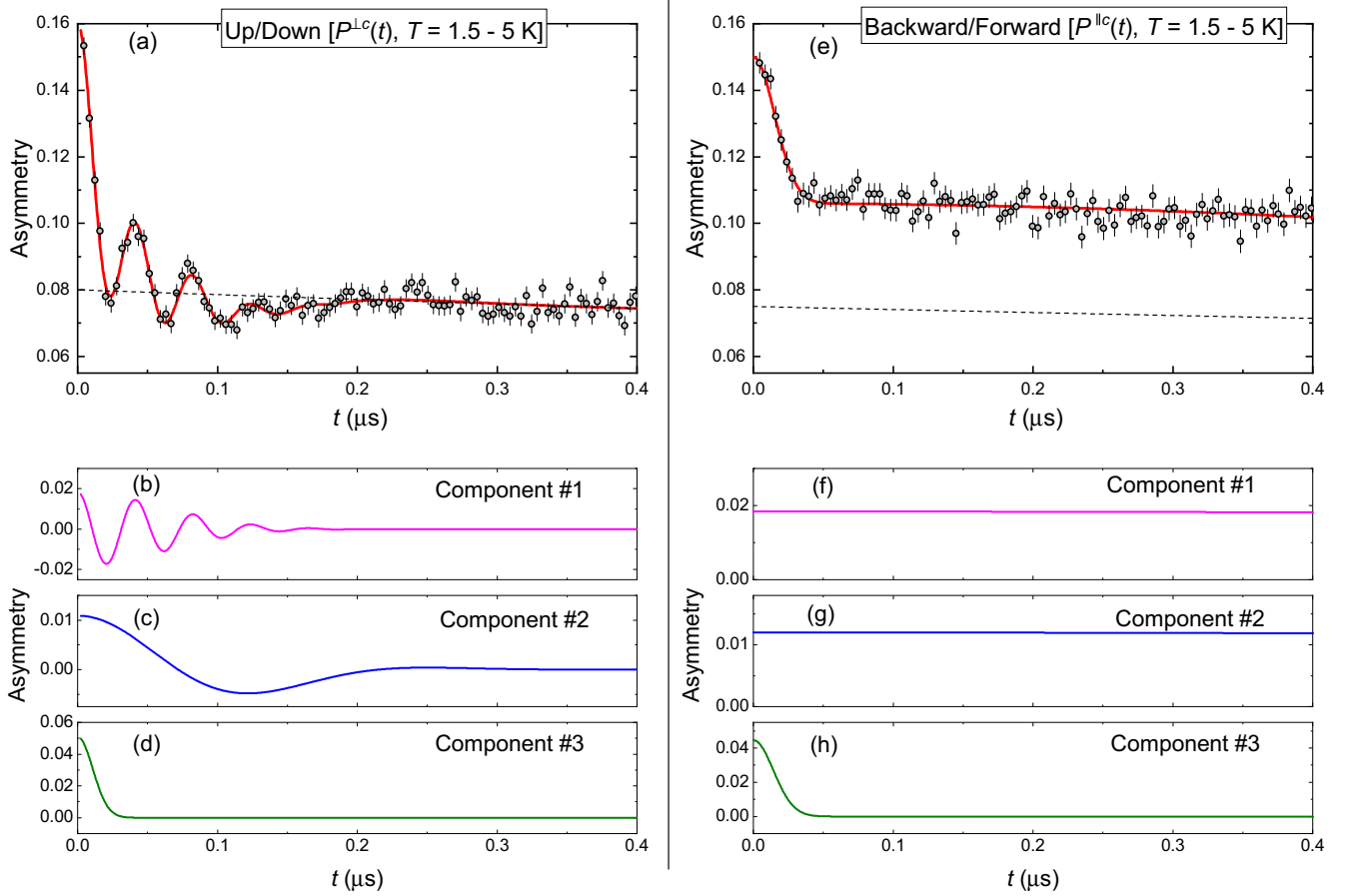
FIG. 5. (a) ZF-$\mu$SR time spectra of $CaK(Fe_{0.949}Ni_{0.051})_4As_4$ measured on up/down set of positron counters. The experiment probes the time evolution of $P^{\perp c}$ component of the muon spin polarization. In order to improve statistics, the data sets collected at temperatures ranging from 1.5 up to 5 K are combined together. The solid line is the fit of Eq. (1) with the sample part described by Eq. (5) to the data. The dashed line is the time evolution of the background component. (b)–(d) Contributions of components Nos. 1, 2, and 3, respectively. (e) The same as in (a), but for backward/forward set of positron counters. In this experiment the time evolution of $P^{\parallel c}$ component of the muon spin polarization is probed. (f)–(h) Represent contributions of the first, second, and third components, respectively.

of magnetically ordered samples $B_{int}$ is directly proportional to the value of the ordered magnetic moments [Fe moments in a case of $CaK(Fe_{0.949}Ni_{0.051})_4As_4$ studied here]. Consequently, the temperature dependence of $B_{int}$ reflects precisely the temperature evolution of the magnetic order parameter $B_{int} \propto m_{Fe}$.

The temperature dependence of $B_{int,1}$ is shown in Fig. 6. The fit was performed globally. In this case, Eq. (1) was fit to the full set of ZF up/down data with certain parameters kept global and some of them remaining individual

for each particular data set. The "global" parameters were the initial asymmetries [$A_1(0)$, $A_2(0)$, $A_3(0)$] and the ratio between the internal fields ($B_{int,2}/B_{int,1}$). The individual parameters were $B_{int,1}$, and the relaxation rates $\sigma_1$ and $\sigma_3$. Note that the preliminary fit with all the parameters remaining "free" reveal that the relaxation rates $\sigma_1$ and $\sigma_2$ stay almost equal. So it was assumed, additionally, $\sigma_1 = \sigma_2$. Above the magnetic transition, a weak Gauss-Kubo-Toyabe damping of the signal was observed caused by the dipole-dipole interaction of the muon magnetic moment with randomly oriented

TABLE I. Parameters obtained from the fit of ZF-$\mu$SR time spectra of $CaK(Fe_{0.949}Ni_{0.051})_4As_4$. The meaning of the parameters is as follows: $B_{int,i}$ is the internal field, $f_i$ is the volume fraction [$f_i = A_i(0)/\{A_1(0) + A_2(0) + A_3(0)\}$], and $\sigma_i$ is the Gaussian relaxation rate of the $i$th component, respectively.

| Polarization component | Detector set | $B_{int}$ (mT) | | | Volume fraction | | | Relaxation rate ($\mu s^{-1}$) | | |
|---|---|---|---|---|---|---|---|---|---|---|
| | | $B_{int,1}$ | $B_{int,2}$ | $B_{int,3}$ | $f_1$ | $f_2$ | $f_3$ | $\sigma_1$ | $\sigma_2$ | $\sigma_3$ |
| $P^{\perp c}$ | Up/down | 177.2(1.5) | 25.7(1.3) | 0 | 0.23(2) | 0.15(1) | 0.62(6) | 16.3(1.4) | 9.7(1.2) | 92.8(7.4) |
| $P^{\parallel c}$ | Backward/forward | 0 | 0 | 0 | 0.25[a] | 0.16[a] | 0.59(7) | 0.39(6) | 0.39(6) | 69.9(5.3) |

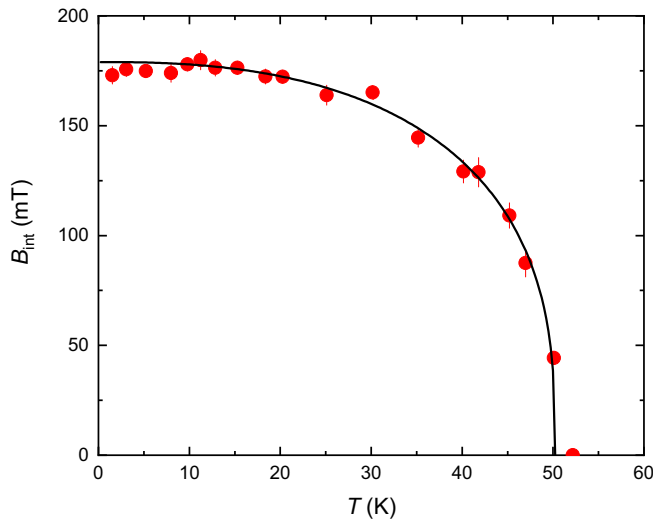[a]The ratio between $f_1$ and $f_2$ was kept the same as for $P^{\perp c}$ set of experiments.

FIG. 6. Temperature dependence of the internal field $B_{int,1}$. The solid line is the fit of Eq. (6) to the data with the parameters $T_N = 50.2(3)$ K, $\alpha = 2.52(9)$, $\beta = 0.35(2)$, and $B_{int}(0) = 179(1)$ mT.

nuclear magnetic moments in the paramagnetic temperature regime.

The results presented in Fig. 6 imply that the onset temperature of the long-range magnetic order, corresponding to decreasing $B_{int}$ down to zero, is consistent with the results of resistivity and the neutron scattering experiments of Kreyssig *et al.* [15], as well as with the results of wTF-$\mu$SR measurements presented in Sec. III A. The temperature dependence of $B_{int}$ is characteristic of a second-order phase transition, consistent with the results of heat capacity, $^{75}$As nuclear magnetic resonance (NMR), neutron scattering, and Mössbauer spectroscopy experiments [12–15].

The temperature dependence of $B_{int}(T)$ was analyzed using a fit to the temperature-dependent magnetic order parameter of the form [33]

$$B_{int}(T) = B_{int}(0)\left[1 - \left(\frac{T}{T_N}\right)^\alpha\right]^\beta. \qquad (6)$$

The fit was made by considering points above the superconducting transition temperature $T_c \simeq 9$ K. The small reduction of $B_{int}$ below $T_c$ is caused by interaction between the magnetic and superconducting order parameters and it is discussed later. The fit yields $T_N = 50.2(3)$ K, $\alpha = 2.52(9)$, $\beta = 0.35(2)$, and $B_{int}(0) = 179(1)$ mT. The value of the effective critical exponent $\beta$ lies quite close to the critical exponent $\beta = 0.325$ expected for a three-dimensional (3D) magnetic system (3D Ising universality class) [34].

## IV. DISCUSSION

### A. Consistency of ZF-$\mu$SR results with the "hedgehog"-type of magnetic order

The results of Sec. III B 1 reveal the presence of three contributions to the time evolution of the muon spin polarization (see components Nos. 1, 2, and 3 in Fig. 5 and Table I). Considering the results of muon-site calculations

presented in Sec. II C, these three components could be further assigned to three different muon stopping sites within the unit cell of $CaK(Fe_{1-x}Ni_x)_4As_4$. Internal fields at two muon stopping positions (components Nos. 1 and 2) are aligned along the crystallographic $c$ direction, while the very broad distribution of fields with the average value centered at zero (component No. 3) corresponds to the third muon position.

The symmetry analysis calculations presented in Appendix A considers eight different magnetic spin-vortex-crystal (SVC) structures with orthogonal iron moments lying in the $ab$ plane. The structures were presented by magnetic order parameters from one-dimensional irreducible representations $\tau 1 - \tau 8$. The SVC structures were divided into two groups with so-called "hedgehog" and "loop" motif in accordance with its orthogonal arrangement of the spin pattern [13]. The SVC structures preserve the C4 symmetry and become consistent with the tetragonal lattice symmetry.

The results of Appendix A exclude the "loop" SVC structures from consideration. With four "hedgehog" SVC magnetic structures left, the one, corresponding to the $\tau 1$ irreducible representation, results in two different fields at the muon stopping sites $\mu 2$ and $\mu 3$ and the zero field on the site $\mu 1$, respectively. The rest gives the single field either at the site $\mu 2$ ($\tau_4$) or $\mu 1$ ($\tau_5$ and $\tau_8$) and zero fields at the muon sites left (see Table II in Appendix A). In all cases, only $z$ component is present, which corresponds to an alignment of the internal magnetic field on the muon position along the crystallographic $c$ direction.

By comparing these results with the ZF-$\mu$SR data (see Fig. 5 and Table I), we conclude that only one single type of the magnetic structure becomes consistent with the experiment. This is the SVC structure with the hedgehog motif corresponding to the $\tau 1$ irreducible representation. The arrangement of Fe moments is presented in Fig. 7. This structure is characterized by noncollinear Fe moments featuring an alternating all-in and all-out motif around the As1 sites within the $ab$ planes and antiferromagnetic coupling along the $c$ direction. Overall, this structure is fully consistent with that reported in NMR, Mössbauer, and neutron scattering experiments [13,15].

Following results presented in Appendix A, the components Nos. 1, 2, and 3 of ZF-$\mu$SR signal (see Sec. III B 1 and Fig. 5) could be assigned to $\mu 2$, $\mu 3$, and $\mu 1$ muon stopping sites, respectively. Three important points need to be considered:

(i) The calculations predict the dipolar fields at the first and the second muon stopping sites resulting in $B_{int,\mu 2} \simeq 366$ mT per $1\mu_B$ and $B_{int,\mu 3} \simeq 94$ mT per $1\mu_B$, respectively ($\mu_B$ is the Bohr magneton). By averaging over the experimentally measured $B_{int,1} \simeq 177.2$ mT and $B_{int,2} \simeq 25.7$ mT (see Table I) the value of the ordered Fe moments is found to be $m_{Fe} = 0.38(0.11)\mu_B$. Such value stays in agreement with $m_{Fe} = 0.37(10)\mu_B$ obtained in neutron scattering experiments [15].

(ii) The fact that the values of the magnetic moment obtained from $B_{int,1}$ ($m_{Fe} \simeq 0.48 \mu_B$) and $B_{int,2}$ ($m_{Fe} \simeq 0.27 \mu_B$) are $\simeq 45\%$ different could be explained by taking into account that calculations consider only the local dipolar fields and
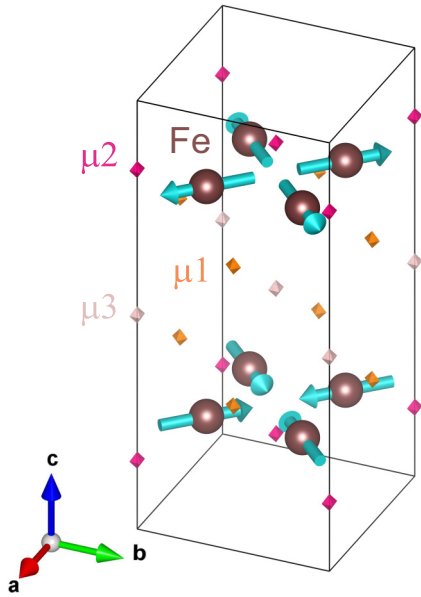
FIG. 7. The magnetic structure of CaK(Fe$_{1-x}$Ni$_x$)$_4$As$_4$ which is consistent with the results of ZF-$\mu$SR measurements. Only the magnetic (Fe) ions are shown. Arrows represent the ordered Fe moments. Diamond symbols correspond to different muon stopping sites. The magnetic unit cell (*P4/mbm* group representation) is doubled and 45° rotated in the *ab* plane with respect to the crystallographic one (*P4/mmm* group representation). See Appendix A for details. The structure is visualized by using VESTA package [18].

neglect contact hyperfine contributions. Similar differences were found, e.g., in La$_2$CuO$_4$ [35], $R$FeAsO ($R$ = La, Ce, Pr, and Sm) [36], Ba$_{1-x}$K$_x$Fe$_2$As$_2$ [29], Ba$_{1-x}$Na$_x$Fe$_2$As$_2$ [30], MnP [37,38], etc.

(iii) The occupancy of the muon stopping sites predicted by calculations is $\mu1 \rightarrow \mu2 \rightarrow \mu3$. Experiment reveals the volume fractions of the first, second, and third components of ZF-$\mu$SR signal to follow: $f_3 \rightarrow f_1 \rightarrow f_2$ (see Table I). Considering the correspondence of the components Nos. 3, 1, and 2 of ZF-$\mu$SR signal to the muon stopping sites $\mu1$, $\mu2$, and $\mu3$ (see the discussion above), this leads to an additional agreement between the theory and the experiment.

We believe that this peculiar, noncollinear SVC magnetic phase is stabilized by the specific crystal structure of 1144 system. Following Meier *et al.* [13] magnetism arising from Fermi surface nesting in the 1144 structure is notably different from the majority of Fe-SC's. The details of its chemical structure and space group break the degeneracy between the pairs of relevant antiferromagnetic orders. For most Fe-SC's such magnetism is characterized by double-degenerate magnetic order parameters leading to formation of the stripe-type magnetic order. The reduced symmetry in the 1144 structure breaks some of this degeneracy and favors the formation of the spin-vortex type of the magnetic order.

## B. Coexistence of superconductivity and magnetism in CaK(Fe$_{0.949}$Ni$_{0.051}$)$_4$As$_4$

Theory works of Fernandes *et al.* [39], Vorontsov *et al.* [40], and Schmiedt *et al.* [41] reveal that magnetism in Fe-based superconductors may coexist with superconductivity.

As a result, a commensurate spin-density wave (SDW) can coexist with a superconducting $s\pm$ state. In the case of coexistence of magnetic order and superconductivity, an interaction between both order parameters is expected. This may change the magnitude of the order parameters and alter the critical temperatures with respect to the decoupled situation.

Here, we used the approach of Machida [17], who has considered the coexistence of spin-density-wave (SDW) type of magnetism with superconductivity within the three-dimensional single-band case. The model was recently employed by Bud'ko *et al.* [14] with the possible application to the multiple-band materials as, e.g., CaK(Fe$_{0.949}$Ni$_{0.051}$)$_4$As$_4$ studied here. Within this model the SDW order is assumed to develop over a nested part of the Fermi surface whereas the superconductivity forms over the full Fermi surface(s).

### 1. Temperature dependence of the magnetic order parameter

Following Refs. [14,17] the superconducting ($\Delta$) and the magnetic ($M$) order parameters could be obtained by solving the system of two coupled self-consistent equations:

$$\ln \frac{T}{T_{s0}} = 2\pi T \sum_{\omega>0}^{\omega_s} \left[ \frac{1}{2M} \left( \frac{M+\Delta}{\sqrt{\omega^2 + (M+\Delta)^2}} + \frac{M-\Delta}{\sqrt{\omega^2 + (M-\Delta)^2}} \right) - \frac{1}{\omega} \right] \quad (7)$$

and

$$\ln \frac{T}{T_{c0}} = n_1 2\pi T \sum_{\omega>0}^{\omega_D} \left[ \frac{1}{2\Delta} \left( \frac{\Delta+M}{\sqrt{\omega^2 + (\Delta+M)^2}} + \frac{\Delta-M}{\sqrt{\omega^2 + (\Delta-M)^2}} \right) - \frac{1}{\omega} \right] + n_2 2\pi T \sum_{\omega>0}^{\omega_D} \left( \frac{1}{\sqrt{\omega^2 + \Delta^2}} - \frac{1}{\omega} \right). \quad (8)$$

Here, $\omega = \pi T (2n+1)$ are Matsubara frequencies with a positive integer $n$, $\omega_D$ is the Debye frequency, $\omega_s$ is a corresponding limit for SDW, $T_{s0}$ is the SDW ordering temperature, $T_{c0}$ is the superconducting transition temperature in absence of magnetism, $n_1$ is partial density of states (DOS) on the Fermi surface part responsible for SDW, and $n_2 = 1 - n_1$. The sums in Eqs. (7) and (8) are convergent and for $\omega_D \gg T_{c0}$ and $\omega_s \gg T_{s0}$ the upper limits of summation can be extended to infinity. Only the case when first the magnetic and then the superconducting order sets in, i.e., for $T_{s0} > T_{c0}$, is considered.

The comparison of Machida's approach with the temperature evolution of the magnetic order parameter obtained in this study is shown in Fig. 8. The $m_{Fe}(T)$ dependence was obtained by normalizing the $B_{int}(T)$ curve (Fig. 6) to $m_{Fe}(20 \text{ K}) = 0.37\mu_B$ as obtained by Kreyssig *et al.* [15] in neutron scattering experiments. The parameters of the modeled curve are $T_{s0}/T_{c0} = 2$ and $n_1 = 0.35$. Note that the theory captures all major features of the experimentally obtained $m_{Fe}(T)$. The initial increase below $T_N \simeq 51$ K, the saturation in $30 \gtrsim T \gtrsim 10$ K temperature region, and the slight drop below the superconducting transition temperature $T_c \simeq 9$ K (see the inset in Fig. 8) are reproduced quite precisely.
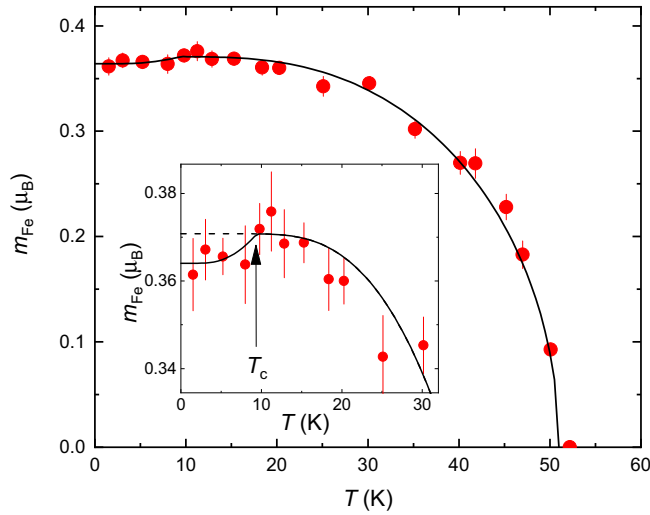
FIG. 8. Temperature dependence of the magnetic order parameter $m_{Fe}$ of $CaK(Fe_{0.949}Ni_{0.051})_4As_4$. The solid line is the analysis by using the approach of Machida [14,17]. The inset shows extension of the low-temperature part. The position of the superconducting transition temperature $T_c$ is marked by the arrow.

It should be noted here that the theory of Machida does not allow to get a "unique" value of the fitting parameters (see also the analysis of Mössbauer spectroscopy data from Ref. [14]). Similar $m_{Fe}(T)$ curves could be obtained with the different set of parameters. As is stressed already in Ref. [14], a unique determination of fit parameters would require additional boundary conditions on them.

### *2. Suppression of the magnetic order parameter in the superconducting state*

The theory of Machida allows to obtain the reduction of the magnetic order parameter in the presence of superconductivity. Calculations presented in Appendix B show that at the limit of $T \to 0$, Eqs. (7) and (8) transform to

$$(m + \delta) \ln(m + \delta) + (m - \delta) \ln(|m - \delta|) = 0 \quad (9)$$

and

$$\delta \ln(\delta\, T_{s0}/T_{c0}) + n_1 [(m + \delta) \ln(m + \delta) - d \ln \delta] = 0. \quad (10)$$

Here, $\delta$ and $m$ are dimensionless superconducting and magnetic order parameters defined as $\delta = \Delta(T = 0)/M_0$ and $m = M(T = 0)/M_0$ ($M_0$ is the zero-temperature value of the magnetic order parameter in the absence of superconducting order). Solutions for $m$ vs $\delta$ values follow the blue solid line presented in Fig. 9. The upper part of the curve corresponds to the monotonic decrease of $m$ with increasing $\delta$. By approaching the point $\delta \simeq 0.55$, $m \simeq 0.67$, the tendency changes. With further decreasing $m$, $\delta$ decreases as well, by approaching $\delta \simeq 0.37$ at $m = 0$. The theory also predicts that $\delta$ remains always smaller than 1 and that the maximum value it may achieve corresponds to $\delta \simeq 0.55$ at $m \simeq 0.7$. This suggests that the magnetism is more robust than superconductivity and that the presence of nearly negligible magnetic contribution (see the point $\delta \simeq 0.37$ for $m \to 0$) is enough to suppress partially the superconductivity.
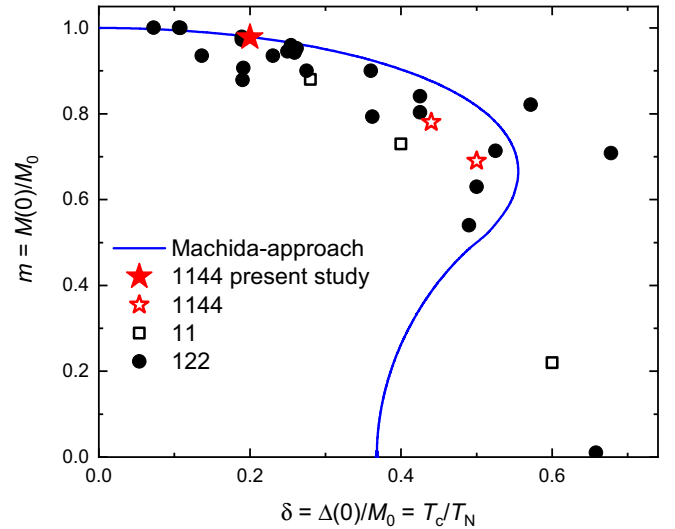


FIG. 9. Dependence of the normalized magnetic $m = M(0)/M_0$ vs the superconducting order parameter $\delta = \Delta(0)/M_0$ obtained within the framework of Machida approach [17] [$M_0$ is the zero-temperature value of the magnetic order parameter in absence of superconductivity, while $M(0) = M(T = 0)$ and $\Delta(0) = \Delta(T = 0)$ are $T = 0$ values of the magnetic and the superconducting order parameters, respectively]. The closed and open stars are experimental points obtained within present studies and by means of Mössbauer spectroscopy and neutron scattering experiments in $CaK(Fe_{1-x}Ni_x)_4As_4$ (1144 family of Fe-SC's) [14,15]. The open squares and closed circles are the experimental data for samples belonging to 11 [42,43] and 122 families of Fe-SC's [30,44–57], respectively.

Comparison with the experimental data could be made by taking into account that within the Machida's approach:

$$\delta = \frac{\Delta(T = 0)}{M_0} = \frac{T_c}{T_{s0}} = \frac{T_c}{T_N}. \quad (11)$$

The closed and open symbols in Fig. 9 correspond to the experimental data for various Fe-SC's belonging to 1144 [as $CaK(Fe_{0.949}Ni_{0.051})_4As_4$] [14,15], 11 [42,43], and 122 families [30,44–57]. The closed star corresponds to the sample studied here. The other data were obtained from the results of neutron scattering, Mössbauer, NMR, and $\mu$SR experiments. The cases when the appearance of superconductivity had visual influence on the temperature evolution of the magnetic order parameter were considered. This, normally, occurs close to the boundary between the magnetic and superconducting regimes.

Qualitatively, the experimental data presented in Fig. 9 follow the upper branch of $m$ vs $\delta$ curve. The question remains as to whether or not the lower part of the curve ($m \lesssim 0.65$) is just a nonphysical solution of the theory or it may correspond to something not yet experimentally observed. One could assume that varying certain external parameters as, e.g., pressure or density of impurities, may allow to verify all these features of Machida's model.

At the end of this section we would mention that the reduction of the magnetic order parameter as a function of $T_c/T_N$ for 122 family of Fe-SC's was studied by Materne *et al.* [57] based on a Landau theory for coupled superconducting

and magnetic order parameters. A quadratic relation between $M(0)/M_0$ and $T_c/T_N$ was reported. Note, however, that the Landau approach used in Ref. [57] requires knowledge of four parameters.

## V. CONCLUSIONS

The zero-field (ZF) and weak transverse-field (wTF) muon spin rotation/relaxation experiments on $CaK(Fe_{0.949}Ni_{0.051})_4As_4$ single-crystal sample were performed. The main results could be summarized as follows:

(i) The sharp transition to the magnetic state with the ordering temperature $T_N = 50.0(5)$ K in both ZF and wTF-$\mu$SR experiments is detected. The value of $T_N$ is found to be in agreement with 50.0(6) K obtained in resistivity, specific heat, and neutron scattering experiments on samples with the similar doping level [12,13,15].

(ii) The calculation of the muon-stopping sites and the symmetry analysis allow to identify the type of the magnetic order in $CaK(Fe_{1-x}Ni_x)_4As_4$. The long-range magnetic spin-vortex-crystal order with the hedgehog motif within the $ab$ plane and the antiferromagnetic stacking along the $c$ direction agrees with the experiment. The value of the ordered magnetic moment was estimated to be $m_{Fe} = 0.38(11)\mu_B$ in agreement with $0.37(10)\mu_B$ from neutron scattering experiments [15]. The type of the magnetic order is the same as determined in NMR, Mössbauer spectroscopy, and neutron scattering experiments [13,15].

(iii) A reduction of the magnetic order parameter below the superconducting transition was detected. The temperature evolution of the magnetic order parameter $m_{Fe}(T)$ is well reproduced within the approach of Machida [14,17], which accounts for coexistence of a spin-density-wave magnetism and superconductivity.

(iv) The theory of Machida was further applied in order to follow the interplay/coexistence of the magnetic and superconducting order parameters for $T$ approaching zero. Comparison with the experiment reveals that the data points for various Fe-based superconducting materials belonging to three different families reproduces reasonably well only the upper branch of $M(0)/M_0$ vs $T_c/T_N$ curve. The question on whether or not the lower part of the curve [$M(0)/M_0 \lesssim 0.65$] corresponds to a nonphysical solution or it has not yet been experimentally detected, remains unexplored.

## APPENDIX A: DIPOLAR FIELDS AT THE MUON STOPPING SITES

The dipolar field analysis follows the procedure described in the Supplemental Material part of Refs. [29,30].

The single- and double-$Q$ magnetic structures which can arise in the $P4/mmm$ setting with $\boldsymbol{Q}_1 = (\frac{1}{2}, \frac{1}{2}, 0)$ and $\boldsymbol{Q}_2 = (-\frac{1}{2}, \frac{1}{2}, 0)$ were considered. For convenience, the crystal structure of $CaKFe_4As_4$ was described within the space group $P4/mbm$ (N127) [the subgroup of indices 2 of the parent group $P4/mmm$ (N123) with doubled unit cell]. The $P4/mbm$ subgroup has the same origin as the parent group $P4/mmm$ and the basis $(a, b, c)$ rotated in the $ab$ plane on 45° compared to the basis $(a', b', c')$ of the $P4/mmm$, so that $a = b = \sqrt{2}a'$ and $c = c'$ (see Fig. 1). In $P4/mbm$ setting, the muon sites become $\mu1$–$4f$ (0,0.5, 0.301); $\mu2$–$4e$ (0,0, 0.186); and $\mu3$–$2b$ (0,0,0.5). The primitive cell of $CaKFe_4As_4$ and descriptions of all ion and muon positions in $P4/mbm$ setting are given in Fig. 10. Note that within the $P4/mbm$ representation used here the magnetic and the crystallographic structures share the similar unit cell. In such a case the symmetry treatment for the Fe- and muon-site magnetic representations could be performed for the propagation vector $\boldsymbol{K}_0 = (0, 0, 0)$.

Eight different double-$Q$ magnetic spin-vortex-crystal (SVC) structures with orthogonal Fe moments lying in the
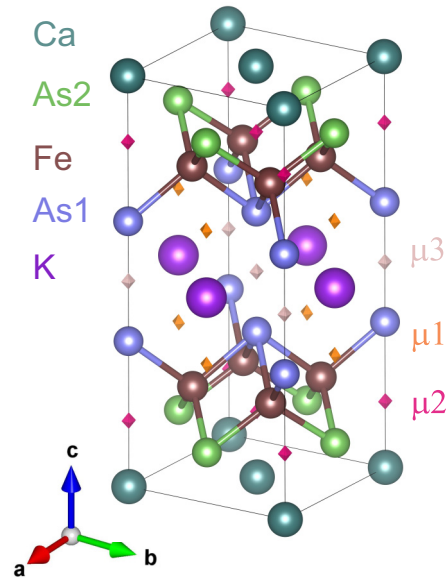


FIG. 10. The crystal structure of $CaKFe_4As_4$ and the muon stopping sites $\mu1$, $\mu2$, and $\mu3$ within the tetragonal subgroup $P4/mbm$ (N127) of the space group $P4/mmm$ (N123). The $P4/mbm$ subgroup has the same origin as the parent group $P4/mmm$ and the basis $(a, b, c)$ rotated in the $ab$ plane on 45° compared to the basis $(a', b', c')$ of the $P4/mmm$. Atoms and muon stopping sites are at the following positions: Ca, $2a$ (0,0,0); K, $2c$ (0,0.5,0.5); As1, $4e$ (0,0,0.35408); As2, $4f$ (0,0.5,0.12310); Fe, $8k$ (0.25, 0.75, 0.76800); $\mu1$–$4f$ (0,0.5, 0.301); $\mu2$–$4e$ (0,0, 0.186); and $\mu3$–$2b$ (0,0,0.5). The crystal structure is visualized by using the VESTA package [18].

TABLE II. The results of dipolar field calculations for various spin-vortex-crystal (SVC) magnetic structures of CaKFe$_4$As$_4$. $P4/mbm$ crystal structure with $K_0 = (0; 0; 0)$ magnetic propagation vector were considered. The values of fields at the muon sites were calculated by means of Eqs. (A1)–(A3), assuming that each Fe carries the magnetic moment of $1\mu_B$.

| IR | Fe order parameter | SVC motif | $\mu1$ (4f) Field symmetry | Field value for $1\mu_B$/Fe (mT) | $\mu2$ (4e) Field symmetry | Field value for $1\mu_B$/Fe (mT) | $\mu3$ (2b) Field symmetry | Field value for $1\mu_B$/Fe (mT) |
|---|---|---|---|---|---|---|---|---|
| $\tau_1 - A_{1g}$ | $L_{3x}^{(-)} + L_{1y}^{(-)}$ | Hedgehog | | 0 | $L_{2z}^{(I)}$ | 365.58 | $l_z$ | 94.36 |
| $\tau_2 - A_{1u}$ | $L_{1x}^{(+)} - L_{3y}^{(+)}$ | Loop | $L_{3z}^{(I)}$ | 0 | $L_{3z}^{(I)}$ | 0 | | 0 |
| $\tau_3 - A_{2g}$ | $L_{1x}^{(-)} - L_{3y}^{(-)}$ | Loop | $F_{3z}^{(II)}$ | 0 | $F_z^{(I)}$ | 0 | $m_z$ | 0 |
| $\tau_4 - A_{2u}$ | $L_{3x}^{(+)} + L_{1y}^{(+)}$ | Hedgehog | | 0 | $L_{1z}^{(I)}$ | 356.04 | | 0 |
| $\tau_5 - B_{1g}$ | $L_{3x}^{(-)} - L_{1y}^{(-)}$ | Hedgehog | $L_{2z}^{(II)}$ | 417.66 | | 0 | | 0 |
| $\tau_6 - B_{1u}$ | $L_{1x}^{(+)} + L_{3y}^{(+)}$ | Loop | | 0 | | 0 | | 0 |
| $\tau_7 - B_{2g}$ | $L_{1x}^{(-)} + L_{3y}^{(-)}$ | Loop | | 0 | | 0 | | 0 |
| $\tau_8 - B_{2u}$ | $L_{3x}^{(+)} - L_{1y}^{(+)}$ | Hedgehog | $L_{1z}^{(II)}$ | 414.53 | | 0 | | 0 |

*ab* plane were introduced. They were presented by magnetic order parameters from one-dimensional irreducible representations (IR's) from $\tau_1$ to $\tau_8$. The SVC structures were divided into two groups with so-defined "hedgehog" ($\tau_1$, $\tau_4$, $\tau_5$, and $\tau_8$) and "loop" ($\tau_2$, $\tau_3$, $\tau_6$, $\tau_7$) motif in accordance with its orthogonal arrangement of the spin pattern [13]. In addition to double $Q$, the single-$Q$ magnetic structures with $\tau_9$ and $\tau_{10}$ IR's could be considered (not shown, see Refs. [29,30] for details). The magnetic structures corresponding to $\tau_1$–$\tau_8$ irreversible representations are shown in Figs. 18 and 19 of Ref. [30].

Table II summarizes the outcome of the dipolar field calculations for the magnetic order parameters of CaKFe$_4$As$_4$. The linear combinations of Fe-magnetic moments [$\vec{F}^{(+),(-)}$, $\vec{L}_1^{(+),(-)}$, $\vec{L}_2^{(+),(-)}$, and $\vec{L}_3^{(+),(-)}$] and the staggered magnetic fields at muon sites ($\vec{F}^{I,II}$, $\vec{L}_1^{I,II}$, $\vec{L}_2^{I,II}$, and $\vec{L}_3^{I,II}$) are described in Ref. [30]. The values of magnetic fields at muon stopping sites were calculated by means of Eqs. (A1)–(A3). Values of Fe moments were set to $1\mu_B$.

Fields at $\mu1$ (4f) muon sites with coordinates $(0, 0.5, 0.301)$ are

$$
\begin{pmatrix} B_x \\ B_y \\ B_z \end{pmatrix} = \begin{pmatrix} 0 & 0 & 0 \\ 0 & 0 & 295.33 \\ 0 & 295.33 & 0 \end{pmatrix} \begin{pmatrix} L_{1x}^{(-)} \\ L_{1y}^{(-)} \\ L_{1z}^{(-)} \end{pmatrix} + \begin{pmatrix} 0 & 0 & -295.33 \\ 0 & 0 & 0 \\ -295.33 & 0 & 0 \end{pmatrix} \begin{pmatrix} L_{3x}^{(-)} \\ L_{3y}^{(-)} \\ L_{3z}^{(-)} \end{pmatrix}
$$
$$
+ \begin{pmatrix} 0 & 0 & 0 \\ 0 & 0 & 293.12 \\ 0 & 293.12 & 0 \end{pmatrix} \begin{pmatrix} L_{1x}^{(+)} \\ L_{1y}^{(+)} \\ L_{1z}^{(+)} \end{pmatrix} + \begin{pmatrix} 0 & 0 & -293.12 \\ 0 & 0 & 0 \\ -293.12 & 0 & 0 \end{pmatrix} \begin{pmatrix} L_{3x}^{(+)} \\ L_{3y}^{(+)} \\ L_{3z}^{(+)} \end{pmatrix}. \tag{A1}
$$

The field at one of $\mu2$ (4e) muon sites with coordinates $(0, 0, 0.186)$ is

$$
\begin{pmatrix} B_x \\ B_y \\ B_z \end{pmatrix} = \begin{pmatrix} 0 & 0 & 0 \\ 0 & 0 & 258.51 \\ 0 & 258.51 & 0 \end{pmatrix} \begin{pmatrix} L_{1x}^{(-)} \\ L_{1y}^{(-)} \\ L_{1z}^{(-)} \end{pmatrix} + \begin{pmatrix} 0 & 0 & 258.51 \\ 0 & 0 & 0 \\ 258.51 & 0 & 0 \end{pmatrix} \begin{pmatrix} L_{3x}^{(-)} \\ L_{3y}^{(-)} \\ L_{3z}^{(-)} \end{pmatrix}
$$
$$
+ \begin{pmatrix} 0 & 0 & 0 \\ 0 & 0 & 251.76 \\ 0 & 251.76 & 0 \end{pmatrix} \begin{pmatrix} L_{1x}^{(+)} \\ L_{1y}^{(+)} \\ L_{1z}^{(+)} \end{pmatrix} + \begin{pmatrix} 0 & 0 & 251.76 \\ 0 & 0 & 0 \\ 251.76 & 0 & 0 \end{pmatrix} \begin{pmatrix} L_{3x}^{(+)} \\ L_{3y}^{(+)} \\ L_{3z}^{(+)} \end{pmatrix}. \tag{A2}
$$

Fields at $\mu3$ (2b) muon sites with coordinates $(0, 0, 0.5)$ are

$$
\begin{pmatrix} B_x \\ B_y \\ B_z \end{pmatrix} = \begin{pmatrix} 0 & 0 & 0 \\ 0 & 0 & -66.73 \\ 0 & -66.73 & 0 \end{pmatrix} \begin{pmatrix} L_{1x}^{(-)} \\ L_{1y}^{(-)} \\ L_{1z}^{(-)} \end{pmatrix} + \begin{pmatrix} 0 & 0 & -66.73 \\ 0 & 0 & 0 \\ -66.73 & 0 & 0 \end{pmatrix} \begin{pmatrix} L_{3x}^{(-)} \\ L_{3y}^{(-)} \\ L_{3z}^{(-)} \end{pmatrix}. \tag{A3}
$$

The calculations imply that magnetic structures, with the corresponding $\tau_2$ and $\tau_3$ IR's, cannot be seen at any of three ($4f$, $4e$, and $2b$) muon stopping sites. The structures corresponding to $\tau_6$ and $\tau_7$ IR's may result in nonzero fields at muon sites only for a case of deviation of Fe ions from the starting $8k$ $(0.25, 0.75, z)$ position to $8k$ $(x, x + 0.5, z)$ with $x \neq 0.25$. However, the x-ray diffraction studies were not detecting any lattice distortions in $CaK(Fe_{0.949}Ni_{0.051})_4As_4$ below $T_N \simeq 50$ K [13]. The iron position $8k$ $(0.25, 0.75, z)$ is expected, therefore, to stay unchanged in the magnetic ordered state. These arguments exclude all loop-type SVC structures from the consideration. The differentiation between four hedgehog SVC magnetic structures could be further made by comparing the ZF-$\mu$SR data with the results of calculations presented in Table II.

The symmetry analysis presented in Table II could be applied to determine the hyperfine magnetic fields induced by SVC orders at As1 ($4e$) and As2 ($4f$) ions. The respective staggered magnetic fields will have the same direction and distribution for $\mu2$ and As1 sites, as well as for $\mu3$ and As2 sites. The As-NMR studies reveal the presence of hyperfine fields at As1 and the absence of such a field at As2 ions in the magnetically ordered state in $CaK(Fe_{1-x}Ni_x)_4As_4$ [13]. This is consistent with the $\tau_1$ or $\tau_4$ representations of the hedgehog SVC order.

## APPENDIX B: MACHIDA APPROACH

The Machida's self-consistent gap equations for the coupled magnetic ($M$) and the superconducting ($\Delta$) order parameters are given in Refs. [14,17] [see also Eqs. (7) and (8) in Sec. IVB1]. Here we consider the derivation of $M$ and $\Delta$ at $T = 0$.

The variables used in Machida's theory are described in Sec. IVB1. The pure magnetic order parameter is assumed to satisfy the BCS relation $M_0/T_{s0} = \pi/e^\gamma \approx 1.76$ ($M_0$ is zero-temperature energy gap in the electron spectrum in the absence of superconducting order). It is convenient for our purpose to use dimensionless variables:

$$t = \frac{T}{T_{s0}}, \qquad \delta = \frac{\Delta}{M_0}, \qquad m = \frac{M}{M_0}. \qquad \text{(B1)}$$

Note that these $m$ and $\delta$ differ from those used in Ref. [14]. This normalization is convenient because $m(0) = 1$.

### 1. Solution at $T = 0$

Considering Eq. (7) at $T \to 0$, the sum could be replaced with an integral according to $2\pi T \sum_\omega \to \int_0^{\omega_s} d(\hbar\omega)$. After integration in first two terms and summation in the last term from $n = 0$ to the maximum corresponding to $\omega_s = 2\pi T N_s$, Eq. (7) transforms to

$$\ln \frac{T}{T_{s0}} = \frac{M+\Delta}{2M} \ln \frac{2\omega_s}{M+\Delta} + \frac{M-\Delta}{2M} \ln \frac{2\omega_s}{|M-\Delta|}$$
$$- \ln(4e^\gamma N_s). \qquad \text{(B2)}$$

Here, the standard treatment of

$$2\pi T \sum_{\omega>0}^{\omega_s} \frac{1}{\omega} = \sum_{n=0}^{N_s} \frac{1}{n+1/2} = \psi\left(\frac{3}{2} + N_s\right) - \psi\left(\frac{1}{2}\right)$$
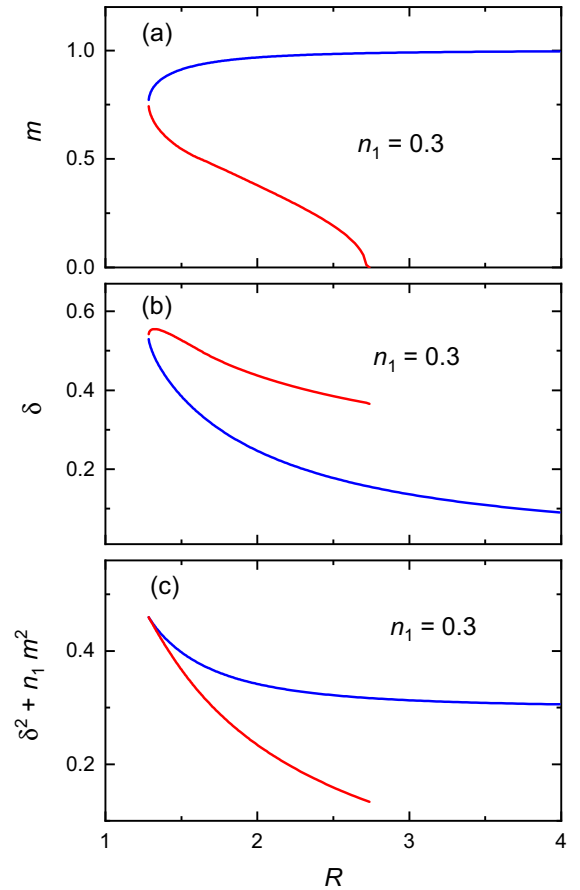
for $N_s \gg 1$ is used.



FIG. 11. (a) $m$ and (b) $\delta$ as a function of the parameter $R = T_{c0}/T_{s0} = \Delta_0/M_0$ corresponding to solutions of the system of Eqs. (B3) and (B5) for $n_1 = 0.3$. The blue (red) branches represent solutions for $m$ increasing (decreasing) as a function of $R$ (see text for details). (c) The $R$ dependence of the quantity $\delta^2 + n_1 m^2$ entering the condensation energy at $T = 0$ [Eq. (B9)].

With the use of dimensionless variables of Eq. (B1), Eq. (B2) is further transformed to

$$(m+\delta)\ln(m+\delta) + (m-\delta)\ln|m-\delta| = 0. \qquad \text{(B3)}$$

In the absence of superconductivity this reduces to $\ln m = 0$, i.e., $m = 1$ and $M(0) = M_0$ as it should.

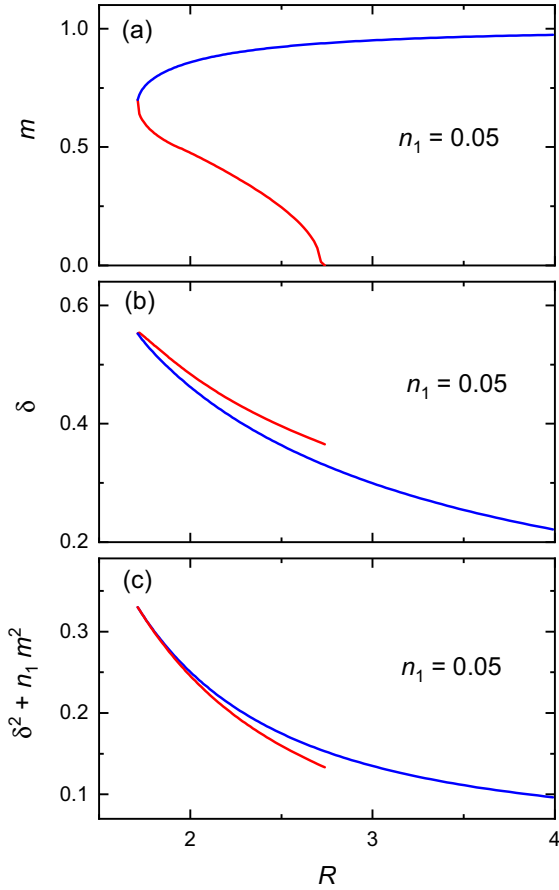Similar manipulations with Eq. (8) give

$$\ln \frac{T}{T_{c0}} = n_1 \left[ \frac{M+\Delta}{2\Delta} \ln \frac{2\omega_D}{M+\Delta} - \frac{M-\Delta}{2\Delta} \ln \frac{2\omega_D}{|M-\Delta|} \right]$$
$$+ n_2 \ln \frac{2\omega_D}{\Delta} - \ln(4e^\gamma N_D), \qquad \text{(B4)}$$

where $N_D = \omega_D/2\pi T$. In dimensionless variables it takes the form

$$n_1 \frac{(m-\delta)\ln|R(m-\delta)| - (m+\delta)\ln[R(m+\delta)]}{2\delta}$$
$$- n_2 \ln(R\delta) = 0. \qquad \text{(B5)}$$

Here,

$$R = \frac{T_{s0}}{T_{c0}} = \frac{M_0}{\Delta_0}$$

FIG. 12. The same as in Fig. 11 but for $n_1 = 0.05$.

and $\Delta_0$ is the superconducting gap in the absence of SDW order. In particular, if $n_1 = 0$, we have $\ln R\delta = 0$, i.e.,

$$R\delta = \frac{M_0}{\Delta_0}\frac{\Delta}{M_0} = \frac{\Delta}{\Delta_0} = 1$$

and $\Delta = \Delta_0$, as it should.

A more compact form of Eq. (B5) is

$$\delta \ln(R\delta) + n_1[(m+\delta)\ln(m+\delta) - \delta \ln \delta] = 0. \quad \text{(B6)}$$

Hence, we have a system of two equations [Eqs. (B3) and (B5)], which can be solved for $m$ and $\delta$ if $n_1$ and $R$ are given. In particular, one can fix $n_1$ and plot $m$ and $\delta$ as a function of $R$ as is done in panels (a) and (b) of Figs. 11 and 12 for $n_1 = 0.3$ and 0.05. Two solution branches, corresponding to the increase and decrease of $m$ with increasing $R$, are represented by blue and red color, respectively.

Similar calculations can be performed by keeping the parameter $R$ constant and evaluating $n_1$ (not shown).

### 2. Solution boundaries

One can get insight to numerical procedure of solving the system of equations for $m$ and $\delta$ by noting that Eq. (B3) does not contain material parameters $R$ and $n_1$, i.e., it is universal. Consider the left-hand side of this equation as a function $\Phi(m, \delta)$ one may plot a contour $\Phi(m, \delta) = 0$. Figures 13 and 14 represent such contours as a red/blue curve. The separation of $m(\delta)$ on the "red" and the "blue" branches is the
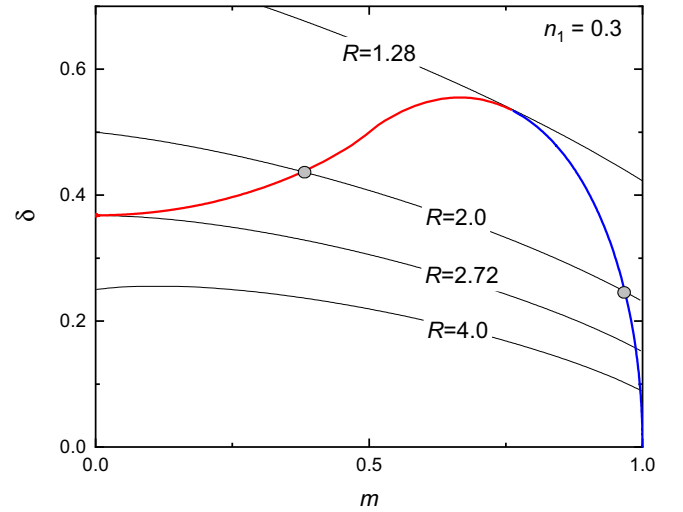


FIG. 13. Solutions of Eqs. (B3) and (B5). Points $(m, \delta)$ on the red/blue curve are solutions of (B3). The black curves are contours of constant $R$'s calculated with the help of Eq. (B5) [or Eq. (B6)] for $n_1 = 0.3$. The points, where two curves cross, correspond to solutions of the system of Eqs. (B3) and (B5).

same as for $m(R)$'s presented in Figs. 11 and 12 for $n_1 = 0.3$ and 0.05, respectively.

Points $\delta$ vs $m$ at these curves satisfy Eq. (B3). In particular, if the superconductivity is completely suppressed, $\delta = 0$, and $\Phi(m, 0) = 2m \ln m = 0$ yields $m = 1$ (the point $\delta = 0$ and $m = 1$ is the rightmost edge of the blue curve at Figs. 13 and 14).

In order to obtain the left edge, i.e., the limit of small $m$ at finite $\delta$, one expands $\Phi$ in powers of $m$:

$$(\delta + m)(\ln \delta + m/\delta) + (m - \delta)(\ln \delta - m/\delta)$$
$$= 2m(\ln \delta + 1) = 0. \quad \text{(B7)}$$

Hence, at small $m$ we have $\delta = 1/e \approx 0.368$, that confirms the numerical result for the leftmost edge of the red/blue curve.
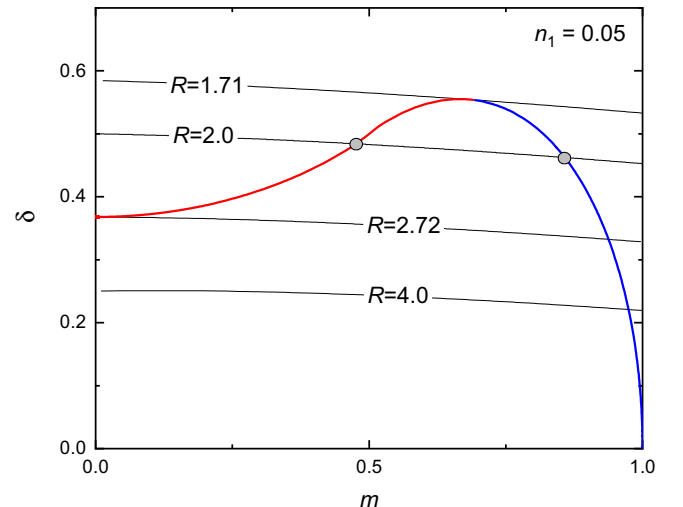


FIG. 14. The same as in Fig. 13, but for $n_1 = 0.05$.

The second equation of the system, Eq. (B6), can be written as

$$R = \exp\left[-\frac{(1-n_1)\delta \ln\delta + n_1(m+\delta)\ln(m+\delta)}{\delta}\right]. \quad \text{(B8)}$$

One can now plot contours of $R(m, \delta, n_1) = $ const for a fixed $n_1$, e.g., for $n_1 = 0.3$ (Fig. 13), on the same graph. In such a case the solutions of both equations are at the points where the red/blue curve crosses contours of constant $R$ (see, e.g., the gray points for $R = 2$ curve). As expected, the contour touch the left edge of $m(\delta)$ curve corresponds to $R = e = 2.718$. Following the data presented in Fig. 11, there are no solutions at all if $R \lesssim 1.28$, there is a single solution for $R \simeq 1.28$, there are two solutions for $1.28 \lesssim R < e \approx 2.72$, and only one solution if $R > e$.

A similar situation is shown in Fig. 14 for $n_1 = 0.05$: no solutions for $R \lesssim 1.7$, two solutions in the interval $1.7 \lesssim R < e \approx 2.72$, and a single solution for $R > e$.

### 3. Condensation energy

Within Machida's model, the condensation energy of both phases at $T = 0$ is

$$\frac{N(0)\Delta^2(0)}{2} + \frac{N_1 M^2(0)}{2} = \frac{N(0)M_0^2}{2}(\delta^2 + n_1 m^2). \quad \text{(B9)}$$

Here, $N_1$ is the density of states (DOS) on the Fermi-surface part responsible for SDW and $N(0)$ is the full DOS.

Figures 11(c) and 12(c) compare the condensation energies for two types of solutions as they are represented by the blue and red curves, respectively. Obviously, in the region where two solutions for a given DOS $n_1$ are possible, $(m_1, \delta_1)$ and $(m_2, \delta_2)$, the blue curve stays above the red one. By decreasing $n_1$, the difference between them decreases and both of them will coincide at the limit of $n_1 \to 0$, i.e., for a case when the magnetism completely vanishes. The question remains whether or not the $m$ vs $\delta$ solutions corresponding to the red part of the curve are just nonphysical or correspond to something observable.

[1] Y. Kamihara, T. Watanabe, M. Hirano, and H. Hosono, J. Am. Chem. Soc. **130**, 3296 (2008).

[2] F.-C. Hsu, J.-Y. Luo, K.-W. Yeh, T.-K. Chen, T.-W. Huang, P. M. Wu, Y.-C. Lee, Y.-L. Huang, Y.-Y. Chu, D.-C. Yan, and M.-K. Wu, Proc. Natl. Acad. Sci. USA **105**, 14262 (2008).

[3] G. R. Stewart, Rev. Mod. Phys. **83**, 1589 (2011).

[4] X. Chen, P. Dai, D. Feng, T. Xiang, and F. C. Zhang, Nat. Sci. Rev. **1**, 371 (2014).

[5] J. Paglione and R. L. Greene, Nat. Phys. **6**, 645 (2010).

[6] R. Khasanov, S. Sanna, G. Prando, Z. Shermadini, M. Bendele, A. Amato, P. Carretta, R. De Renzi, J. Karpinski, S. Katrych, H. Luetkens, and N. D. Zhigadlo, Phys. Rev. B **84**, 100501(R) (2011).

[7] R. Khasanov, R. M. Fernandes, G. Simutis, Z. Guguchia, A. Amato, H. Luetkens, E. Morenzoni, X. Dong, F. Zhou, and Z. Zhao, Phys. Rev. B **97**, 224510 (2018).

[8] J. G. Bednorz and K. A. Muller, Z. Phys. B **64**, 189 (1986).

[9] A. Iyo, K. Kawashima, T. Kinjo, T. Nishio, S. Ishida, H. Fujihisa, Y. Gotoh, K. Kihou, H. Eisaki, and Y. Yoshida, J. Am. Chem. Soc. **138**, 3410 (2016).

[10] W. R. Meier, T. Kong, U. S. Kaluarachchi, V. Taufour, N. H. Jo, G. Drachuck, A. E. Böhmer, S. M. Saunders, A. Sapkota, A. Kreyssig, M. A. Tanatar, R. Prozorov, A. I. Goldman, F. F. Balakirev, A. Gurevich, S. L. Bud'ko, and P. C. Canfield, Phys. Rev. B **94**, 064501 (2016).

[11] W. R. Meier, T. Kong, S. L. Bud'ko, and P. C. Canfield, Phys. Rev. Materials **1**, 013401 (2017).

[12] W. R. Meier, Ph.D. thesis, Growth, properties and magnetism of CaKFe$_4$As$_4$, Iowa State University, Ames, USA, 2018.

[13] W. R. Meier, Q.-P. Ding, A. Kreyssig, S. L. Bud'ko, A. Sapkota, K. Kothapalli, V. Borisov, R. Valenti, C. D. Batista, P. P. Orth, R. M. Fernandes, A. I. Goldman, Y. Furukawa, A. E. Böhmer, and P. C. Canfield, npj Quantum Mater. **3**, 5 (2018).

[14] S. L. Bud'ko, V. G. Kogan, R. Prozorov, W. R. Meier, M. Xu, and P. C. Canfield, Phys. Rev. B **98**, 144520 (2018).

[15] A. Kreyssig, J. M. Wilde, A. E. Böhmer, W. Tian, W. R. Meier, Bing Li, B. G. Ueland, Mingyu Xu, S. L. Bud'ko, P. C. Canfield, R. J. McQueeney, and A. I. Goldman, Phys. Rev. B **97**, 224521 (2018).

[16] Q.-P. Ding, W. R. Meier, A. E. Böhmer, S. L. Bud'ko, P. C. Canfield, and Y. Furukawa, Phys. Rev. B **96**, 220510(R) (2017).

[17] K. Machida, J. Phys. Soc. Jpn. **50**, 2195 (1981).

[18] K. Momma and F. Izumi, J. Appl. Crystallogr. **44**, 1272 (2011).

[19] A. Amato, H. Luetkens, K. Sedlak, A. Stoykov, R. Scheuermann, M. Elender, A. Raselli, and D. Graf, Rev. Sci. Instrum. **88**, 093301 (2017).

[20] R. Khasanov, H. Zhou, A. Amato, Z. Guguchia, E. Morenzoni, X. Dong, G. Zhang, and Z. Zhao, Phys. Rev. B **93**, 224512 (2016).

[21] A. Schenck, *Muon Spin Rotation Spectroscopy: Principles and Applications in Solid State Physics* (Adam Hilger Ltd., Bristol, UK, 1985).

[22] S. L. Lee, R. Cywinski, and S. H. Kilcoyne, *Muon Science: Proceedings of the 51st Scottish Universities Summer School in Physics: NATO Advanced Study Institute on Muon Science, 1728 August, 1998* (Institute of Physics, Bristol, UK, 1999).

[23] J. H. Brewer, Muon Spin Rotation/Relaxation/Resonance, in *Encyclopedia of Applied Physics*, edited by G. L. Trigg (VCH, New York, 1994), Vol. 11, p. 23.

[24] A. Yaouanc, and P. Dalmas de Réotier, *Muon Spin Rotation, Relaxation and Resonance: Applications to Condensed Matter* (Oxford University Press, Oxford, 2011).

[25] A. Suter and B. M. Wojek, Phys. Procedia **30**, 69 (2012).

[26] ELK code, 2009, http://elk.sourceforge.net.

[27] J. P. Perdew and Y. Wang, Phys. Rev. B **45**, 13244 (1992).

[28] J. P. Perdew, A. Ruzsinszky, G. I. Csonka, O. A. Vydrov, G. E. Scuseria, L. A. Constantin, X. Zhou, and K. Burke, Phys. Rev. Lett. **100**, 136406 (2008).

[29] B. P. P. Mallett, Y. G. Pashkevich, A. Gusev, T. Wolf, and C. Bernhard, Europhys. Lett. **111**, 57001 (2015).

[30] E. Sheveleva, B. Xu, P. Marsik, F. Lyzwa, B. P. P. Mallett, K. Willa, C. Meingast, Th. Wolf, T. Shevtsova, Yu. G. Pashkevich, and C. Bernhard, Phys. Rev. B **101**, 224515 (2020).

[31] R. Khasanov, Z. Guguchia, I. Eremin, H. Luetkens, A. Amato, P. K. Biswas, C. Rüegg, M. A. Susner, A. S. Sefat, N. D. Zhigadlo, E. Morenzoni *et al.*, Sci. Rep. **5**, 13788 (2015).

[32] R. Khasanov, A. Shengelaya, D. Di Castro, E. Morenzoni, A. Maisuradze, I. M. Savić, K. Conder, E. Pomjakushina, A. Bussmann-Holder, and H. Keller, Phys. Rev. Lett. **101**, 077001 (2008).

[33] F. L. Pratt, P. M. Zieliński, M. Balanda, R. Podgajny, T. Wasiutyński, and B. Sieklucka, J. Phys.: Condens. Matter **19**, 456208 (2007).

[34] L. J. De Jongh and A. R. Miedema, Adv. Phys. **23**, 1 (1974).

[35] H.-H. Klauss, J. Phys.: Condens. Matter **16**, S4457 (2004).

[36] H. Maeter, H. Luetkens, Yu. G. Pashkevich, A. Kwadrin, R. Khasanov, A. Amato, A. A. Gusev, K. V. Lamonova, D. A. Chervinskii, R. Klingeler, C. Hess, G. Behr, B. Büchner, and H.-H. Klauss, Phys. Rev. B **80**, 094524 (2009).

[37] R. Khasanov, A. Amato, P. Bonfà, Z. Guguchia, H. Luetkens, E. Morenzoni, R. De Renzi, and N. D. Zhigadlo, Phys. Rev. B **93**, 180509(R) (2016).

[38] R. Khasanov, A. Amato, P. Bonfà, Z. Guguchia, H. Luetkens, E. Morenzoni, R. De Renzi, and N. D. Zhigadlo, J. Phys.: Condens. Matter **29**, 164003 (2017).

[39] R. M. Fernandes, D. K. Pratt, W. Tian, J. Zarestky, A. Kreyssig, S. Nandi, M. G. Kim, A. Thaler, N. Ni, P. C. Canfield, R. J. McQueeney, J. Schmalian, and A. I. Goldman, Phys. Rev. B **81**, 140501(R) (2010).

[40] A. B. Vorontsov, M. G. Vavilov, and A. V. Chubukov, Phys. Rev. B **81**, 174538 (2010).

[41] J. Schmiedt, P. M. R. Brydon, and C. Timm, Phys. Rev. B **89**, 054515 (2014).

[42] M. Bendele, A. Amato, K. Conder, M. Elender, H. Keller, H.-H. Klauss, H. Luetkens, E. Pomjakushina, A. Raselli, and R. Khasanov, Phys. Rev. Lett. **104**, 087003 (2010).

[43] M. Bendele, A. Ichsanow, Yu. Pashkevich, L. Keller, Th. Strässle, A. Gusev, E. Pomjakushina, K. Conder, R. Khasanov, and H. Keller, Phys. Rev. B **85**, 064517 (2012).

[44] A. I. Goldman, D. N. Argyriou, B. Ouladdiaf, T. Chatterji, A. Kreyssig, S. Nandi, N. Ni, S. L. Bud'ko, P. C. Canfield, and R. J. McQueeney, Phys. Rev. B **78**, 100506(R) (2008).

[45] S. Avci, O. Chmaissem, E. A. Goremychkin, S. Rosenkranz, J.-P. Castellan, D. Y. Chung, I. S. Todorov, J. A. Schlueter, H. Claus, M. G. Kanatzidis, A. Daoud-Aladine, D. Khalyavin, and R. Osborn, Phys. Rev. B **83**, 172503 (2011).

[46] M. G. Kim, D. K. Pratt, G. E. Rustan, W. Tian, J. L. Zarestky, A. Thaler, S. L. Bud'ko, P. C. Canfield, R. J. McQueeney, A. Kreyssig, and A. I. Goldman, Phys. Rev. B **83**, 054514 (2011).

[47] A. Kreyssig, M. G. Kim, S. Nandi, D. K. Pratt, W. Tian, J. L. Zarestky, N. Ni, A. Thaler, S. L. Bud'ko, P. C. Canfield, R. J. McQueeney, and A. I. Goldman, Phys. Rev. B **81**, 134512 (2010).

[48] P. Wang, Z. M. Stadnik, J. Zukrowski, A. Thaler, S. L. Bud'ko, and P. C. Canfield, Phys. Rev. B **84**, 024509 (2011).

[49] H. Luo, R. Zhang, M. Laver, Z. Yamani, M. Wang, X. Lu, M. Wang, Y. Chen, S. Li, S. Chang, J. W. Lynn, and P. Dai, Phys. Rev. Lett. **108**, 247002 (2012).

[50] S. Nandi, M. G. Kim, A. Kreyssig, R. M. Fernandes, D. K. Pratt, A. Thaler, N. Ni, S. L. Bud'ko, P. C. Canfield, J. Schmalian, R. J. McQueeney, and A. I. Goldman, Phys. Rev. Lett. **104**, 057006 (2010).

[51] P. Marsik, K. W. Kim, A. Dubroka, M. Rössle, V. K. Malik, L. Schulz, C. N. Wang, C. Niedermayer, A. J. Drew, M. Willis, T. Wolf, and C. Bernhard, Phys. Rev. Lett. **105**, 057001 (2010).

[52] A. D. Christianson, M. D. Lumsden, S. E. Nagler, G. J. MacDougall, M. A. McGuire, A. S. Sefat, R. Jin, B. C. Sales, and D. Mandrus, Phys. Rev. Lett. **103**, 087002 (2009).

[53] D. K. Pratt, M. G. Kim, A. Kreyssig, Y. B. Lee, G. S. Tucker, A. Thaler, W. Tian, J. L. Zarestky, S. L. Bud'ko, P. C. Canfield, B. N. Harmon, A. I. Goldman, and R. J. McQueeney, Phys. Rev. Lett. **106**, 257001 (2011).

[54] C. Bernhard, C. N. Wang, L. Nuccio, L. Schulz, O. Zaharko, J. Larsen, C. Aristizabal, M. Willis, A. J. Drew, G. D. Varma, T. Wolf, and Ch. Niedermayer, Phys. Rev. B **86**, 184509 (2012).

[55] Z. Li, R. Zhou, Y. Liu, D. L. Sun, J. Yang, C. T. Lin, and G.-Q. Zheng, Phys. Rev. B **86**, 180501(R) (2012).

[56] R. Zhou, Z. Li, J. Yang, D. L. Sun, C. T. Lin, and G.-Q. Zheng, Nat. Commun. **4**, 2265 (2013).

[57] P. Materne, S. Kamusella, R. Sarkar, T. Goltz, J. Spehling, H. Maeter, L. Harnagea, S. Wurmehl, B. Büchner, H. Luetkens, C. Timm, and H.-H. Klauss, Phys. Rev. B **92**, 134511 (2015).